nature communications

Article

https://doi.org/10.1038/s41467-026-70940-z

Frequent floods in the Yangtze River basin linked to a shifted Indian Ocean wave regime

Received: 22 July 2025

Accepted: 6 March 2026

Published online: 26 March 2026

Check for updates

Panini Dasgupta [1], SungHyun Nam [1,2,3] ✉, Michael J. McPhaden [4] ✉, Dong-Jin Kang [5,6], J. S. Saranya [1] & M. K. Roxy [7]

Six major summer monsoon floods occurred in the Yangtze Basin during 1992–2024 compared to only one during 1960–1991. This significant increase in hydroclimatic extremes, which affected millions of people, is closely linked to a 50% enhancement in quasi-biennial variability in East Asian summer monsoon rainfall and associated Yangtze River discharge. This quasi-biennial variability is strongly coupled with intensified tropical baroclinic wave activity in the Indian Ocean under enhanced ENSO forcing. During the later period, amplified westward propagating downwelling baroclinic Rossby waves in late boreal spring and summer strongly suppressed vertical mixing and entrainment in the western tropical Indian Ocean, maintaining anomalously warm sea surface temperatures. This anomalously warm ocean enhanced local atmospheric convection and tropospheric heating, which remotely strengthened the western Pacific subtropical high via atmospheric Kelvin wave processes, thereby increasing moisture transport and summer monsoon rainfall over the Yangtze River Basin. A 70% increase in the phase speed of the baroclinic Rossby waves during the later period also favoured the seasonal phase locking of ocean wave–driven tropical Indian Ocean warming with the East Asian summer monsoon.

In the years following a positive Indian Ocean Dipole (IOD) (occurring with or without a positive phase of the El Niño–Southern Oscillation, ENSO), anomalously warm sea surface temperature (SST) in the western tropical Indian Ocean and associated enhanced convection exert a strong influence on the East Asian summer monsoon (EASM) circulation by modifying the position and strength of western Pacific subtropical high (WPSH)[1–6]. This often leads to catastrophic flooding in the Yangtze River Basin[2]. Notable summer monsoon flood events in the past three decades occurred in 1995, 1996, 1998, 1999, 2016, and most recently, in 2020. Beyond affecting millions of people, extreme discharge from the Yangtze River also exerts a profound impact on the marine environment of the East Asian Marginal Seas, with lasting consequences for fisheries and coastal economies in the following season[6,7]. The physical mechanisms responsible for the anomalously warm western tropical Indian Ocean during late spring and early summer, preceding the onset of the East Asian summer monsoon, are still not well resolved. In some years, such warming is followed by the development of positive ENSO and IOD events[5,8,9], as seen in 1998 and 2016. In other years, such as 2020, similar warm SST anomalies develop following a positive IOD without a concurrent significant ENSO signal[2]. While many studies interpret SST anomalies as a result of coupled ocean–atmosphere feedback[10], others highlight the dominant role of ocean dynamics over atmospheric processes in initiating them[2,9–11].

[1]Future Innovation Institute, Seoul National University, Siheung, Republic of Korea. [2]School of Earth and Environmental Sciences, College of Natural Sciences, Seoul National University, Seoul, Republic of Korea. [3]Research Institute of Oceanography, College of Natural Sciences, Seoul National University, Seoul, Republic of Korea. [4]Pacific Marine Environmental Laboratory, National Oceanic and Atmospheric Administration, Seattle, WA, USA. [5]Department of Ocean Science, University of Science and Technology, Daejeon, Republic of Korea. [6]Office of the Vice President, Korea Institute of Ocean Science and Technology, Busan, Republic of Korea. [7]Centre for Climate Change Research, Indian Institute of Tropical Meteorology, Ministry of Earth Sciences, Pune, India. ✉e-mail: namsh@snu.ac.kr; michael.j.mcphaden@noaa.gov

The dominant tropical Indian Ocean modes namely, IOD and the Indian Ocean Basin (IOB) mode are tightly coupled to tropical wave dynamics, specifically the equatorial Kelvin (fast component) and Rossby (slow component) wave components[12,13]. The strength of these waves is often significantly modulated by ENSO-driven anomalous wind stress curl forcing. In particular, the forced Rossby waves strongly interact with those reflected from the eastern boundary, influencing the overall westward propagation of energy across the basin[14,15]. While the Kelvin–Rossby (K–R) wave cycle is impacted by ENSO timescales, its intrinsic or natural frequency lies predominantly in the quasi-biennial (QB) band (1.2–3 years or ~14–36 months)[14,16]. Thus, QB-timescale waves are not exclusive to IOD or IOB years, but their amplitudes are markedly enhanced during these events[14]. Menezes and Vianna[14] comprehensively explained how this band captures the leading mode of baroclinic Rossby and Kelvin wave activity in the tropical Indian Ocean. They showed that leading mode variability at QB timescale is highly correlated with the IOD index with correlation coefficients of 0.6 or higher, indicating the dominant role of these waves underlying the IOD phenomena[14]. Notably, earlier studies have also highlighted the QB nature of the EASM[17–20], suggesting a potential dynamical linkage with QB–timescale tropical Indian Ocean wave activity.

Recent studies suggest a fundamental shift in the Indian Ocean's dynamical processes and their coupling with atmospheric variability in recent decades, particularly since the 1990s, as reflected in the rising frequency of "early pIOD" events and the associated EASM extremes[10,19–21]. Concurrently, the QB band of ENSO variability has been reported to strengthen since the 1990s, driven by an increased influence of North Atlantic SST variability associated with the positive phase of the Atlantic Multidecadal Oscillation[22–26]. However, the role of enhanced QB-ENSO variability in modulating tropical Indian Ocean wave dynamics and its downstream impacts on the EASM remains poorly understood. Between 1992 and 2024 (which we designate "Late period"), extreme rainfall events and corresponding Yangtze River Discharge (YRD) under western pole warming increased significantly compared to 1960–1991 (designated "Early period") (Fig. 1a). The rationale for selecting these two contrasting periods is detailed in the Results section. Focusing on the QB band, which captures the dominant tropical Indian Ocean wave signals, this study examines changes in the characteristics of Kelvin and Rossby waves between the two periods and evaluates their subsequent impacts on EASM variability.

Results

Characteristic change in YRD and its association with ENSO, IOD, and IOB

Figure 1a presents the long-term (1960–2024) monthly (black) and seasonal mean (June–July–August –JJA denoting the peak discharge months) (olive) anomalous river discharge (in m^3/s) recorded at the Datong station (30.77°N, 117.62°E), with anomalies calculated by removing the climatological annual cycle based on the entire period. The frequency of extreme discharge events has increased markedly since the 1990s, particularly during 1990–2000 and 2010–2024. In the Early period, above-normal JJA discharge events (exceeding the 75th percentile) occurred in 1962, 1970, 1973, 1977, and 1983, with only 1983 classified as extreme (exceeding the 90th percentile). In contrast, during the Late period, above-normal events were observed in 1993, 1995, 1996, 1998, 1999, 2002, 2010, 2016, 2019, 2020, and more recently in 2024 with 1995, 1996, 1998, 1999, 2016, and 2020—exceeded the 90th percentile, highlighting a substantial rise in both the frequency and intensity of discharge extremes in recent decades (Fig. 1a). An increase in extreme below-normal discharge events is also noted during the Late period relative to the Early period highlighting an increase in the overall variability of EASM rainfall and the associated Yangtze River discharge[27]. It is important to note that, in this study, the term extreme YRD events refers to anomalous seasonal extremes in JJA-mean YRD, rather than to individual river discharge events associated with extreme rainfall. With a monthly resolution dataset, we primarily focus on the interannual variability of river discharge and its extreme anomalies.

The contrast between the Early and Late periods becomes more apparent when focusing on the QB timescale. Figure 1b presents the 3-year rolling standard deviation of QB-filtered (1.2–3 years) YRD (in m^3/s), Yangtze River Basin–averaged rainfall, and the amplitude of the first complex empirical orthogonal function (CEOF) mode derived from ORAS5 sea surface height (SSH). This leading CEOF mode (CEOF1) captures the dominant propagating wave signals in the tropical Indian Ocean, which are discussed in greater detail in the following section. Figure 1b demonstrates that enhanced QB-timescale variability in YRD coincides with extreme discharge events, highlighting the role of QB-scale processes in modulating hydrological extremes. Notably, this QB variability is nonstationary, intensifying markedly after the 1990s. This pronounced increase in QB variability (approximately by 50%) in both rainfall and river discharge over the Yangtze River Basin provides a compelling rationale for defining two distinct periods, Early (1960–1991) and Late (1992–2024), during which the nature of QB variability differs fundamentally. The rolling 3-year mean amplitude of the QB-band SSH CEOF1 also exhibits a marked increase (also approximately by 50%) after the 1990s, closely following the observed variability in QB-scale YRD. Therefore, in remainder of this manuscript, we focus on differences in QB-scale variability in YRD between the Early and Late periods, with particular emphasis on its relationship with Indian Ocean wave dynamics.

Indian Ocean wave activity at QB timescale is known to be strongly amplified associated with the IOD, ENSO, and IOB climate modes, quantified respectively by the Dipole Mode Index (DMI), Niño-3.4 index, and IOB index (see Data Availability)[13,14]. The indices of these climate modes and their lagged influence on the EASM highlight the role of amplified wave dynamics and their broader impacts. Figure 1c and d illustrates how the lagged relationship between these modes and YRD differs between the Early and Late periods. Figure 1c and d shows the lagged correlations of the detrended DMI, Niño 3.4, and IOB indices with detrended monthly YRD across various target months[28]. To isolate the Indian Ocean influence, the ENSO component was removed from the DMI and IOB indices using orthogonal linear regression technique following Jarugula and McPhaden[28]. The orthogonal regression method better captures the linear relationship between two coupled variables that both contain observational errors. The first column of Fig. 1c shows that JJA YRD was most significantly correlated ($r > 0.3$) with the positive IOD at a lag of 8–12 months (i.e., the previous year's July–November) during the Early period, shifting to a lag of 8–10 months (i.e., September–November) in the Late period. This indicates that the impact of pure IOD events on YRD remained consistent between the Early and Late periods; however, the lag between peak positive IOD and above-normal river discharge shortened by approximately one month. The correlations between YRD and both the Niño-3.4 and IOB indices became significantly stronger during the boreal winter and spring months (November–April) in the Late period (second and third columns of Fig. 1c). For the IOB, a positive correlation between the March–May IOB index and July–September River discharge was already present during the Early period; however, in the Late period, the March–May IOB index became more strongly correlated with JJA river discharge, indicating a quicker YRD response to this climate mode by approximately one month. Notably, no consistent lag relationship between ENSO and YRD existed during the Early period, whereas in the Late period this relationship became significantly stronger. These changes suggest a significant enhancement in the coupling between Pacific and Indian Ocean variability and the EASM system during the Late period. The observed changes in the lagged responses of YRD to Indian Ocean variability indicate a shift in the underlying tropical Indian Ocean wave characteristics, while the

enhanced coupling with ENSO further suggests changes in the associated forcing on these waves, which are examined in detail in the subsequent sections.

The surface mixed layers in the Seychelles–Chagos Thermocline Ridge (SCTR) marked by the black box in Fig.2a (enclosed by 55°E–75°E and 12°S–5°S) in the southwestern tropical Indian Ocean and the eastern equatorial Indian Ocean near Java–Sumatra are highly sensitive to baroclinic wave induced shallow thermocline displacements. Atmospheric forcing during IOD and ENSO events is known to energize the K–R wave cycle, resulting in pronounced surface warm anomalies in these regions[10,12]. The lag and intensity of these warm anomalies following the IOD and ENSO depend strongly on the location and strength of the atmospheric forcing, as well as the phase speed of the K–R waves[16,29,30]. Therefore, in the following sections, we primarily concentrated on the characteristics and forcing of these dominant K–R waves which eventually lead to contrasting EASM variability during two periods.

Strengthening of variability the QB band

The lower panels of Supplementary Fig. 1a–1c show the change in standard deviation of ORAS5-SSH, ORAS5 depth of 20 °C isotherms (D20 serves as a well-established proxy for thermocline depth in tropical oceans), and EN4-D20, between the Early and Late periods across three distinct frequency bands: annual (10–14 months), QB

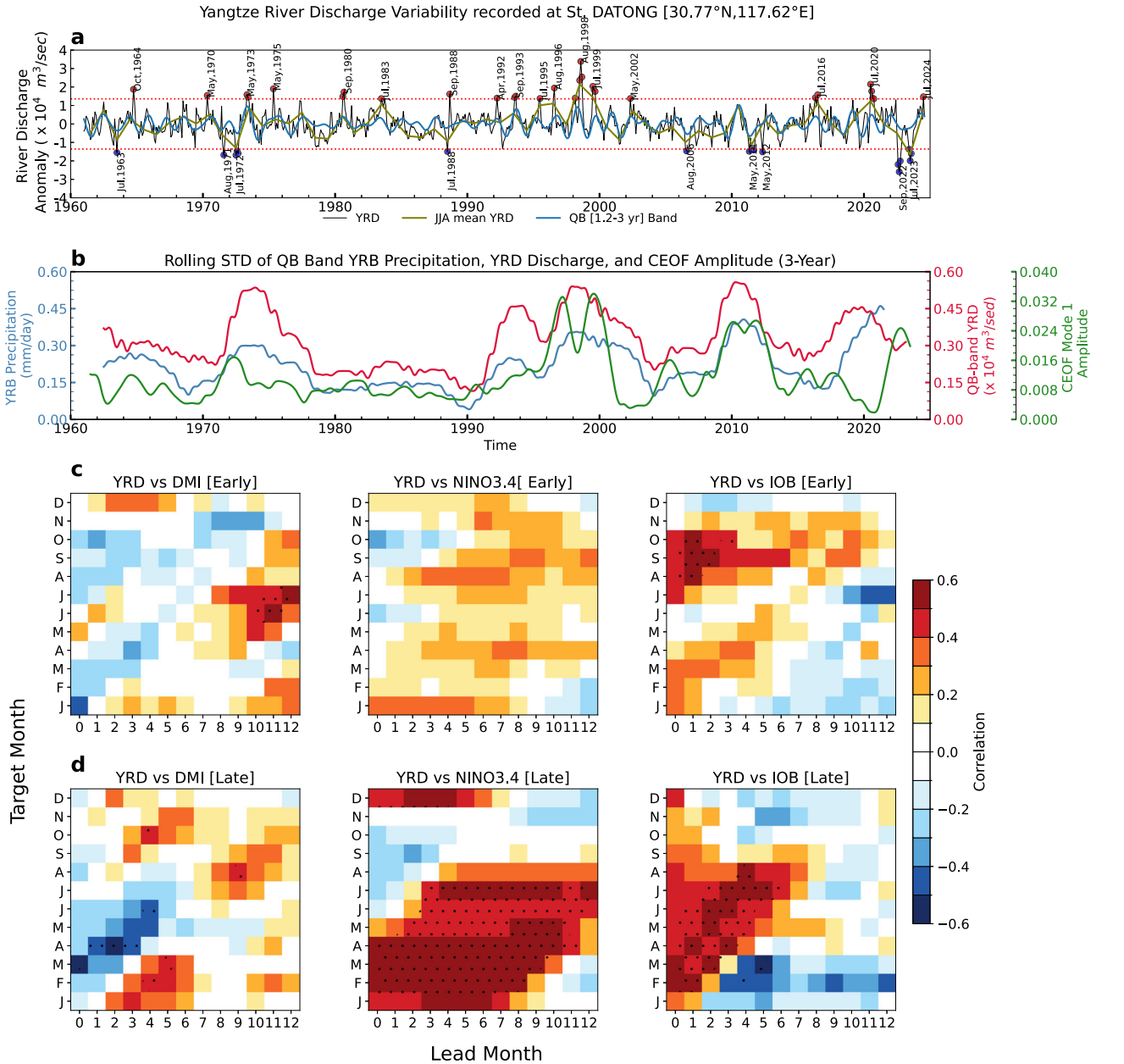

Fig. 1 | Relationship between Yangtze River discharge (YRD) and El Niño–Southern Oscillation (ENSO), Indian Ocean Dipole (IOD), and Indian Ocean Basin (IOB) mode. a Time series of anomalous YRD (m^3/s) recorded at the Datong station (30.77°N, 117.62°E). Extreme discharge years are identified based on a two-standard-deviation threshold from the climatological mean. The blue and olive lines represent the quasi-biennial (QB; 1.2–3 years) and June–August (JJA) mean anomalous river discharge, respectively. **b** Three-year rolling standard deviation of QB Yangtze River Basin precipitation, YRD, and the amplitude of the CEOF1 mode from ORAS5 sea surface height (SSH). **c**, **d** Cross-correlation coefficients (dots represent $p < 0.05$) as a function of lead time and target month, computed between detrended YRD and three detrended climate indices: the Dipole Mode Index (DMI), the Niño 3.4 index, and the IOB index, for the (**c**) Early (1960–1991) and (**d**) Late (1992–2024) periods. The linear effect of the Niño 3.4 index on the DMI and IOB indices was removed using orthogonal regression.

https://doi.org/10.1038/s41467-026-70940-z

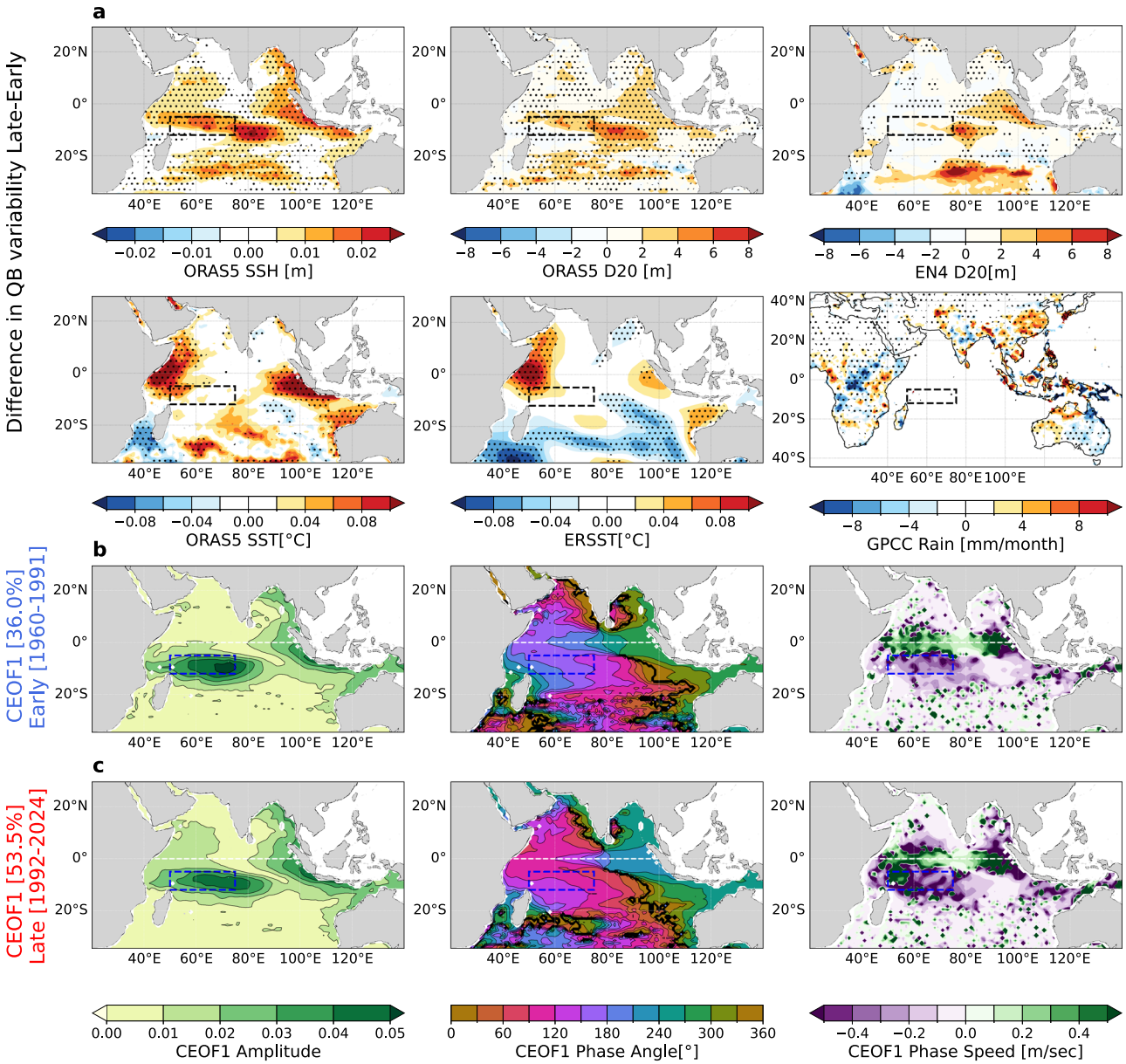

Fig. 2 | Changes in quasi-biennial (QB) variability between the Early (1960–1991) and Late (1992–2024) periods. a Difference in the QB standard deviation between the Late and Early periods for ORAS5 SSH [m], ORAS5 D20 [m], EN4 D20 [m], ORAS5 SST [°C], ERSST SST [°C], and GPCC rainfall [mm/day]. Shaded areas indicate regions where the difference in standard deviation is statistically significant ($p < 0.05$) based on Levene's test, rejecting the null hypothesis of equal variances between the two periods. **b**, **c** Amplitude, phase, and phase speed associated with the leading complex EOF (CEOF1) mode of QB-filtered SSH during the early (**b**) and late (**c**) periods. The region enclosed by the blue and black dashed lines denotes the Seychelles–Chagos Thermocline Ridge region (SCTR; 50°E–75°E, 12°S–5°S).

(14–36 months), and ENSO-scale (36–96 months). Notably, the most pronounced increase is noted in the QB band, primarily observed across the latitudinal band of the SCTR and along the Java–Sumatra coast (upper panel, Fig. 2a). In contrast, for the low-frequency ENSO band, enhanced variability is primarily confined to the SCTR region (Supplementary Fig. 1). Supplementary Figs. 2 and 3, together with the lower panel of Fig. 2a, present the standard deviation of ORAS5-SST, ERSST, CHM rainfall, and GPCC rainfall, (see Data Availability section) similarly filtered into the three frequency bands and compared across the two periods. Notably, among the three frequency bands, SST variability in the tropical Indian Ocean and rainfall variability over the EASM region are most pronounced at the QB timescale. The lower panel of Fig. 2a reveals a substantial increase in QB-SST variability between the Early and Late periods, particularly in both the western and eastern poles of the equatorial Indian Ocean. Moreover, we observed marked enhancement in QB-scale rainfall variability over the EASM region, especially in the Yangtze River Valley (Supplementary Fig. 3 and Fig. 2a).

To examine the propagation characteristics of energetic baroclinic waves in the tropical Indian Ocean, we performed CEOF analysis on QB band-filtered ORAS5 SSH anomalies for the Early and Late periods following Menezes and Vianna[14]. CEOF1 accounted for 36 and 53.5% of the total QB band variance in the Early and Late periods, respectively (Fig. 2b, c), indicating strengthening of the dominant mode approximately by 50% over time along with increased QB variability.

Supplementary Figs. 4 and 5 show the second and third CEOF modes, which captures westward-propagating signals at higher latitudes[14]. Since the total variance explained by these higher-order modes is substantially smaller, our focus here is primarily on the

leading mode and its associated propagation features. Importantly, the temporal evolution of the CEOF1 mode amplitude was also in phase with YRD variability (Fig. 1b), suggesting a potential linkage between leading-mode oceanic wave dynamics and continental hydrological response. The SCTR region exhibits the maximum amplitude of the first propagating mode (Fig. 2b, c). As shown in the first column of Fig. 2b, c, the amplitude structure of CEOF1 becomes more zonally aligned during the Late period, possibly indicating an enhancement in the zonal wavelength. The second column of Fig. 2b, c illustrates the corresponding spatial phase structure, which displays a latitudinally varying westward-propagating pattern, a fundamental characteristic of baroclinic Rossby waves[31]. Notably, the Rossby wavefront in the SCTR region appears sharper in the Late period than in the Early period. The third column of Fig. 2b, c presents the phase speed of CEOF1, computed from spatial and temporal phase gradients. In the equatorial Indian Ocean, the CEOF1 phase speeds are predominantly positive, indicating the presence of eastward-propagating equatorial Kelvin waves. Overall, CEOF1 represents the cycle of K–R waves in the tropical Indian Ocean. Since the Kelvin wave component is very fast and difficult to resolve properly in the monthly ORAS5 and EN4 datasets, we primarily focused on the slow-moving baroclinic Rossby wave component and identified their characteristic changes between the Early and Late periods.

Changes in baroclinic Rossby wave characteristics in the tropical Indian Ocean

We observed a significant increase in the westward phase speed of CEOF1 during the Late period, especially along the SCTR latitude band (Fig. 3a). In Supplementary Fig. 6a, similar phase speed differences were noted using QB-filtered EN4 D20 data. Notably, the eastward phase speed shows a significant increase near the western and eastern boundaries of the equatorial Indian Ocean (Fig. 3a). Although a slight reduction in eastward phase speed can be observed over the central equatorial Indian Ocean, it remains small relative to the high mean phase speed of Kelvin waves. It is important to note though that D20 variations in both ORAS5 and EN4 do not adequately capture equatorial Kelvin wave signals (Supplementary Fig. 5).

Using the entire study period (1960–2024) based CEOF1 (explaining 47% of the total QB-band variance), we identified eight distinct phases of CEOF1 propagation (Figs. 3b and 4a, see Methods for detail explanations). Across all eight phases, we observed a consistent increase in westward phase speed over the SCTR region (derived from the spatial phases over the SCTR), suggesting that both the upwelling and downwelling components of the baroclinic Rossby waves have accelerated in recent decades (Fig. 3b, c see Methods). Notably, variability in the westward SCTR phase speed during phases 4, 5, and 6, corresponding to the downwelling phase, has intensified significantly during the Late period, indicating a greater variability in propagation speed than its upwelling counterpart. Figure 3c presents the temporal evolution of SCTR phase speed and CEOF1 amplitude during 1960–2024, highlighting an intensification in westward phase speed and its variability, along with a larger amplitude since the 1990s. Importantly, these periods of enhanced phase speed coincide with intervals of intensified CEOF1 activity.

To further verify the observed enhancement in westward phase speed, Fig. 3d (upper panel) presents phase–longitude composites of QB-SSH anomalies during active CEOF1 phases (see Methods). Here, we observe that in the Late period, the phase transitions between successive phases occur more rapidly along the longitudes than during the Early period, indicating an acceleration of the wave cycle. To obtain an independent estimate of westward phase speed separate from the CEOF analysis, we present in Fig. 3d (bottom panel) lag composites of SSH anomalies, centred on the time of maximum SSH anomaly in the SCTR region (50°E–75°E, 12°S–5°S), using a threshold of one standard deviation. From these composites, we tracked the time-lag position of the peak anomaly for each longitude between 55°E and 85°E to estimate the mean westward propagation speed. This independent method also confirmed a significant increase (approximately by 70%) in the westward phase speed over the SCTR, from 0.16 m s^{-1} in the Early period to 0.27 m s^{-1} in the Late period. Consistent changes were also observed in the CEOF1 of EN4-D20, as presented in Supplementary Fig. 6d.

Mixed-layer heat balance associated with an amplified and accelerated wave cycle and its downstream impacts on the YRD

The QB-SSH anomalies across the eight CEOF1 phases (Fig. 4a) illustrate the K–R wave cycle during the early and late periods. In the late period, stronger anomalies extend farther zonally across all phases, indicating an enhanced wavelength, consistent with the observed increase in the mean phase speed of the baroclinic Rossby waves. Importantly, the enhanced phase speed and wavelength are also evident in the normalized zonal wavenumber–frequency spectra of SSH anomalies across the Indian Ocean basin (35°E–125°E, 15°S–15°N), where the normalized power is strongly enhanced at zonal wavenumber one during the Late period (Supplementary Fig. 7).

The K–R wave cycle is manifested as major climate modes when amplified as noted by previous studies[12,14]. In Fig. 4a, the propagation of baroclinic waves and their manifestation in QB–SST anomalies are presented. The positive and negative phases of the IOD and IOB appear at different stages of the K–R wave cycle. In Supplementary Fig. 8a and Fig. 4a, we observed that the positive and negative phases of the IOD, denoted by the DMI index above and below one standard deviation, respectively, predominantly occurred during CEOF1 phase 3 and phase 7. Similarly, the active phases of positive and negative IOB predominantly appeared in CEOF1 phases 5 and 1 or 2, respectively. Notably, the QB–SST anomalies closely match the overall detrended SST anomalies across all CEOF1 phases, highlighting the dominant role of the QB-scale K–R wave cycle in interannual SST variability of tropical Indian Ocean (Supplementary Fig. 9).

The faster and zonally longer downwelling baroclinic Rossby waves during the late period (Figs. 3d and 4a) produced anomalous SST warming over a broader area of the tropical Indian Ocean basin, particularly during CEOF1 Phase 6. In this phase, the downwelling Rossby waves exit the SCTR region, initiating thermocline shoaling, while the reflected Kelvin waves deepen the thermocline along the Sumatra–Java coast, thereby activating thermocline–SST feedback processes. During the late period, the amplified and longer downwelling Rossby waves in the SCTR anomalously suppressed vertical entrainment and diffusive mixing at the mixed-layer base due to the reduced vertical temperature gradient associated with a deeper thermocline. Supplementary Figs. 10–12 present the deseasoned and detrended mixed-layer heat budget components across the Indian Ocean basin, derived from ORAS5 for the eight CEOF1 phases during the early and late periods and their differences (see Methods). Consistent with previous studies, subsurface processes largely compensate surface heat fluxes over the SCTR region across most phases[32–36]. The late-minus-early differences (Supplementary Fig. 12) further show that the strongest positive SST tendency in the SCTR occurs during CEOF1 Phase 6 and is dominated by reduced vertical entrainment and diffusive mixing. Moreover, Supplementary Figs. 13 and 14 indicate that this suppression is primarily driven by the weakened vertical temperature gradient associated with a deeper thermocline.

Since the K–R wave cycles are also phase-locked with the seasonal cycle, the probability of certain phases occurring is higher in specific months. The acceleration of the wave cycle significantly alters this probability distribution. In Fig.4b, we presented the joint probability distribution of each active phase, month-wise, for the Early and Late periods. In certain months, this probability was five times higher than the unbiased probability of 0.01 (1/96), denoting the phase-locked wave cycle. It shows the propagation differences of the forced Rossby

https://doi.org/10.1038/s41467-026-70940-z

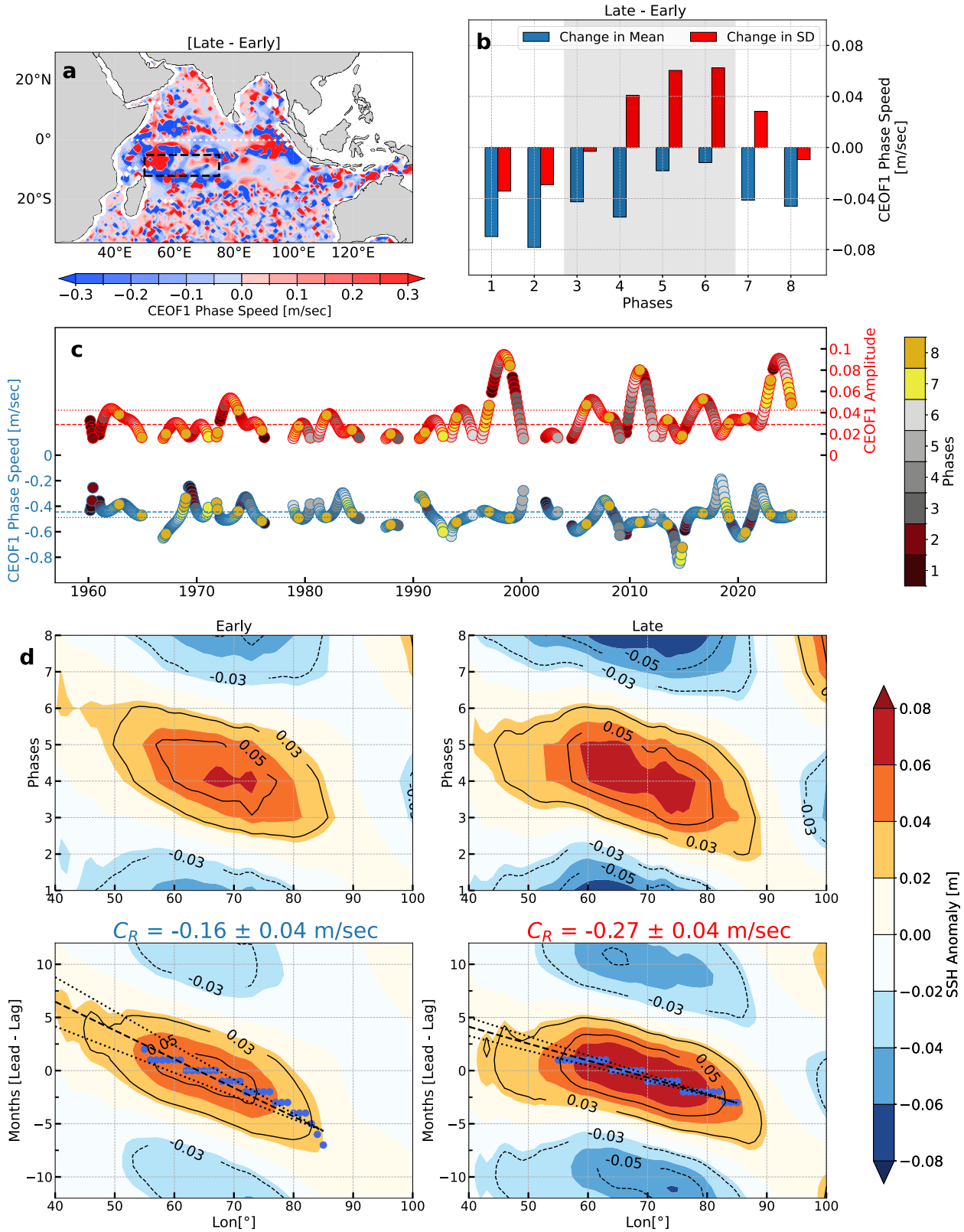

wave signal following the CEOF1 phase 3 (+IOD condition) from the preceding year September–November to phases 5 (+IOB condition) and 6 in the following year June–August. In the Late period, this propagation is considerably faster, with phase 6 emerging ahead of the EASM onset, leading to warmer SST anomalies in the SCTR region. The differences between the Early and Late periods shown in Fig. 4b also largely explain the changes in lag correlations between YRD and IOD and IOB (Fig. 1c, d), where we noted a shorter lag between +IOD (CEOF1 phase 3), +IOB (CEOF1 phase 5) and JJA river discharge (CEOF1 phase 6).

During above- and below-normal YRD years (defined as ±1 standard deviation of JJA discharge), the May–August K–R wave cycle preferentially occupies Phases 6 and 2, respectively, indicating that these phases favor extreme YRD conditions (Supplementary Fig. 8b). This preferential occurrence disappears during normal years, although

Fig. 3 | Changes in the westward phase speed of baroclinic Rossby waves as evident in the leading complex EOF (CEOF1) mode of quasi-biennial timescale sea surface height (QB-SSH) between the Early (1960–1991) and Late (1992–2024) periods. a Changes in the phase speed of the CEOF1 mode [m/sec]. The region enclosed by the black dashed lines denotes the SCTR region (50°E–75°E, 12°S–5°S). **b** Change in the mean and standard deviation of westward CEOF1 phase speed over the SCTR across eight CEOF1 phases. The shaded region denotes the downwelling phases of baroclinic Rossby Waves over the SCTR region. **(c)** Time series of CEOF1 phase speed and the amplitude over the SCTR. Dashed and dotted horizontal lines represent the means for the Early and Late periods. **d** (Top) Hovmöller plot showing longitudinal propagation of QB-SSH anomalies averaged between 5°S and 12°S across eight CEOF phases during. (Bottom) Composite lagged propagation of QB-SSH [m], centred on anomalous peaks (exceeding one standard deviation) over the SCTR. Here, the black dashed line denotes the mean westward phase speed of QB–SSH over the SCTR region, estimated using a best linear fit. The black dotted lines represent the 95% confidence interval of the fitted slope (approximately ± 0.04 m s^{-1} for both periods).

Phases 2 and 6 retain higher probabilities due to seasonally locked propagation. QB-YRD anomalies exhibit their strongest positive correlation with CEOF1 amplitude and strongest negative correlation with CEOF1 phase speed at Phase 6, implying that higher-amplitude, faster K–R waves enhance QB-scale YRD (Supplementary Fig. 8c). This relationship remains robust across both Early and Late periods.

To understand how the anomalous SST in K–R wave-cycle phase 6, impact the QB scale YRD variability dynamically, we presented QB-YRD correlated SSH, SST, SLP, MFD, E–P, and SSS during the Early and Late periods, and their differences between Early and Late period in Fig.5. QB-YRD–correlated SSH anomalies consistently exhibit a K–R wave cycle Phase-6 pattern over the tropical Indian Ocean during both the Early and Late periods, indicating a consistent and robust linkage between K–R wave cycle and QB-YRD variability. The associated SST anomalies across the Indian Ocean basin are strongly coupled to QB-YRD activity, with above-normal YRD events occurring most frequently during Phase 6, during which positive QB-SST correlations over the eastern equatorial Indian Ocean persist in both periods. During the Late period, these correlations expand into the central and western Indian Ocean, coinciding with enhanced warming of the region associated with the faster and amplified wave cycle. The enhanced QB-YRD correlation with central and western tropical Indian Ocean QB-SST anomalies during the Late period is also reflected in a strengthened negative correlation with QB-SLP anomalies over the central–western tropical Indian Ocean, indicating intensified deep convective activity. During anomalously high QB-YRD years in the Late period, enhanced deep convection over the western–central tropical Indian Ocean excites a Matsuno–Gill–type atmospheric response, in which an eastward-propagating equatorial Kelvin wave strengthens the anomalous WPSH and thereby contributes to anomalous YRD events, consistent with the previous literatures on the downstream impacts of tropical Indian Ocean heating[2,37–40]. The QB-scale moisture flux divergence, evaporation–precipitation, and SSS identify the western Indian Ocean, northern Bay of Bengal, and WPSH as key moisture source regions, whose influence becomes more pronounced during the Late period (Fig. 6). Overall, the dynamical linkage between the K–R wave cycle, its associated climate modes, and QB-scale YRD variability remains consistent during the Early and Late periods but intensifies during the Late period due to the amplification and acceleration of the K–R wave cycle (Fig. 1c, d). Supplementary Fig. 15 shows significant phase coherence between QB-SST and QB-YRD over the tropical Indian Ocean even during the Early period, consistent with significant lag correlations between YRD and the IOD–IOB (Fig. 1c, d). During the Late period, this coherence strengthens and extends into the tropical central–eastern Pacific, indicating enhanced Pacific influence. This interpretation is further supported by a strengthened ENSO–YRD relationship in seasonally stratified statistics and a marked increase in QB amplitude over Niño3.4 (Supplementary Fig. 16).

Potential drivers of increased westward phase speed in the SCTR and amplification of the K–R wave cycle

Changes in the ocean stratification, can significantly alter the baroclinic Rossby waves speed[31]. To examine whether changes in ocean stratification contribute to the acceleration of westward phase speed in the SCTR, we estimated the theoretical first baroclinic-mode Rossby wave speed using the WKBJ approximation, derived from the mean buoyancy frequency (N^2) profiles down to 3,500 m at each grid point (see Methods). Zonal (60°E–100°E) and meridional (12°S–5°S) mean profiles of the derived phase speed are shown in Fig. 7a and d, with corresponding spatial distributions in Supplementary Fig. 17. The meridional profiles of phase speed from CEOF1-ORAS5 SSH and CEOF1-D20 EN4 broadly agree with theoretical estimates in both the Early and Late periods. However, the magnitude of the theoretical phase speed change is approximately an order of magnitude smaller (~ 1/10th) than the observed changes in CEOF1 (Fig. 7b, c, e, f), suggesting that changes in stratification alone cannot fully explain the observed acceleration. Likewise, changes in upper ocean circulation also provide no obvious explanation for the acceleration of baroclinic Rossby waves during the Late period (Supplementary Fig. 18a).

The atmospheric forcing, especially between 75°E and 100°E, plays a critical role in modulating Rossby wave propagation and is known to introduce discontinuity in phase speed along these longitudes[16,29,30]. This longitudinal band often acts as a zone for the reinjection or initiation of Rossby waves[14] (Supplementary Fig. 18b). As shown in Supplementary Fig. 18b, wind stress curl variability peaks at the QB timescale and has increased substantially between 75°E and 100°E in the Late period, along within the ENSO band, particularly along 10°S. In Supplementary Fig. 18c, d, we assessed the phase coherence between QB wind stress curl and QB wave signals, using both ORAS5 SSH and EN4 D20 anomalies. Here we note that the phase coherence has increased along the eastern edge of the SCTR (75°E–90°E, 15°S–10°S) in the Late period suggesting an enhanced coherent QB forcings to the southeast of the SCTR are the most probable drivers of the enhanced wave speed, especially along the southern SCTR. The decreased phase coherency at the centre of the SCTR also signifies an accelerated propagation of the forced baroclinic waves, leading to altered seasonal phase locking. Although this study identifies enhanced QB–WSC variability as the most probable drivers of the enhanced phase speed, further focused scientific investigations are required to evaluate and establish this proposed hypothesis.

The enhanced phase coherence between QB Niño3.4 and QB-WSC, and between QB-YRD and QB-WSC, highlights the role of ENSO in strengthening QB–WSC forcing along 75°E–100°E in the tropical Indian Ocean, which likely amplified and accelerated the K–R wave cycle during the Late period (Supplementary Fig. 19). Recent studies suggest that temperature anomalies in the northern tropical Atlantic, coupled with the Atlantic Multidecadal Oscillation, are responsible for the amplification of ENSO biennial variability[22–26].

Discussion

A marked increase in extreme YRD flood events is observed during the Late period (1992–2024) compared to the Early period (1960–1991), coinciding with an approximately 50% enhancement in QB variability of rainfall over the Yangtze River Basin and tropical Indian Ocean wave activity. We find that the lagged relationships between YRD and major climate modes, the IOD, ENSO, and IOB change significantly from the Early to the Late period, driven by pronounced changes in K–R wave characteristics. Although the dynamical linkage between the K–R wave cycle and YRD remains robust throughout the record, it is substantially strengthened during the Late period under enhanced QB–ENSO

https://doi.org/10.1038/s41467-026-70940-z

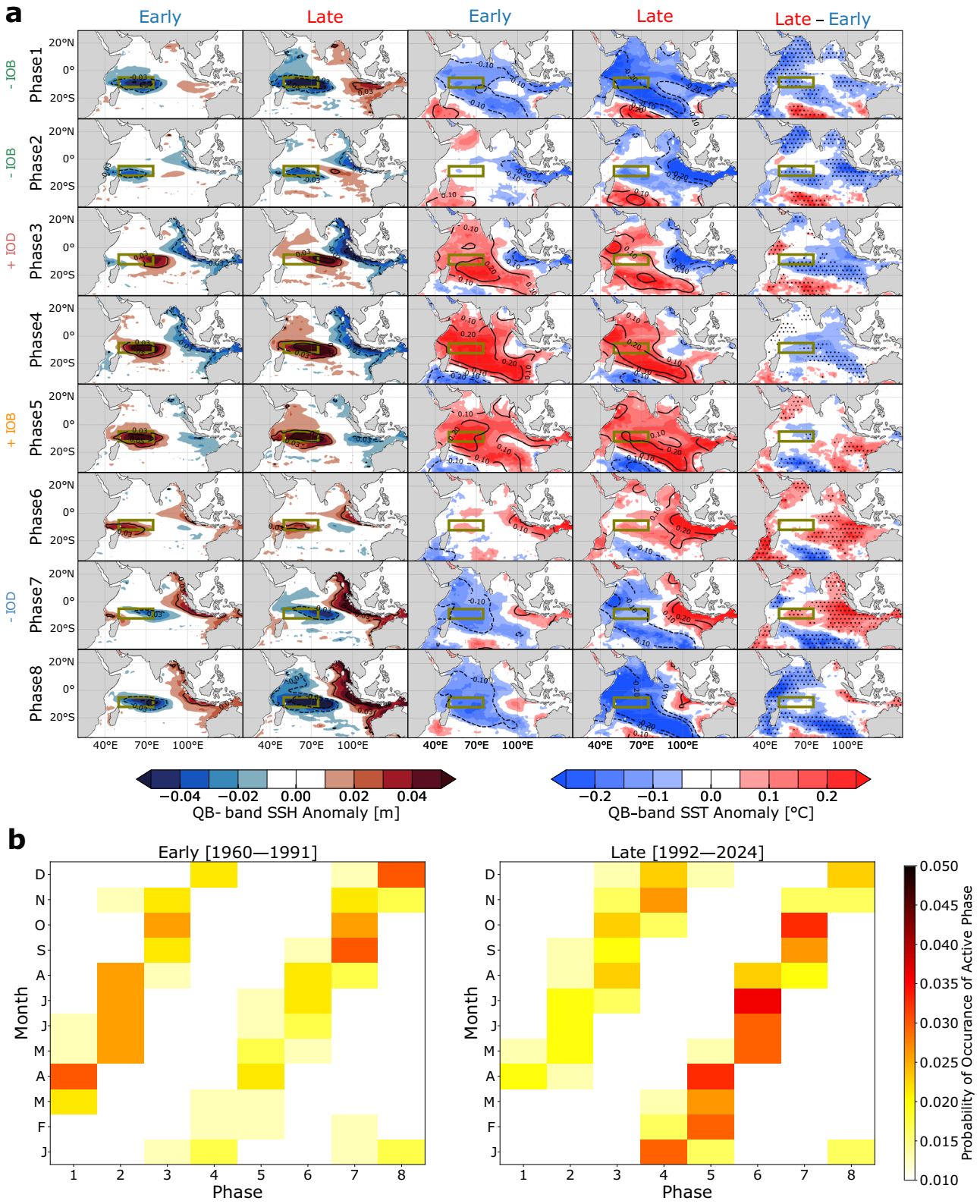

Fig. 4 | Phase evolution of the Kelvin–Rossby (K–R) wave cycle during the Early (1960–1991) and Late (1992–2024) periods. a Composites of QB-SSH [m] and QB–SSTs [°C] for the eight active CEOF1 phases, along with their differences between Early and Late Periods. ERSST is shown as contours and ORAS5 SST as shading. The region enclosed by the olive lines denotes the SCTR region (50°E–75°E, 12°S–5°S). **b** Joint probability distribution of active CEOF1 phase occurrences (defined as CEOF1 amplitude > 25th percentile) across eight CEOF1 phases and twelve calendar months.

https://doi.org/10.1038/s41467-026-70940-z

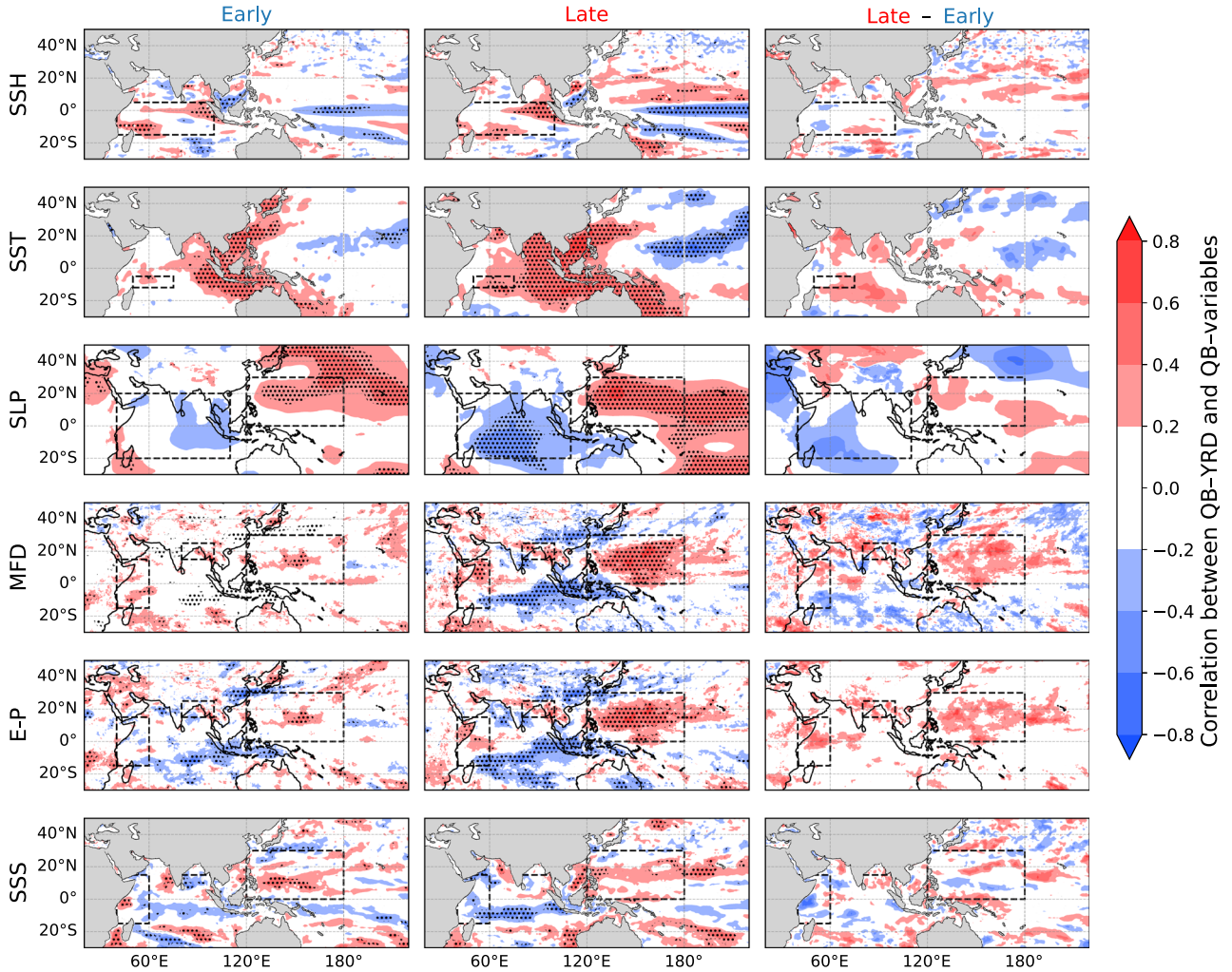

Fig. 5 | Downstream impacts of the Kelvin–Rossby (K–R) wave cycle on quasi-biennial timescale Yangtze River discharge (QB–YRD) during Early (1960–1991) and Late (1992–2024) periods. QB–YRD correlated QB–scale sea surface height (SSH; ORAS5), sea surface temperature (SST; HadISST), mean sea level pressure (SLP; ERA5), moisture flux divergence (MFD; ERA5; negative values indicate convergence leading to enhanced rainfall), evaporation–precipitation (E–P; ERA5), and sea surface salinity (SSS; ORAS5) (top to bottom) during the Early and Late periods, along with their differences. Boxes denote regions relevant to QB–YRD variability in-terms of moisture sources, including the western Pacific subtropical high (WPSH), western tropical Indian Ocean (WTIO), and northern Bay of Bengal (nBOB). Dotted regions indicate statistical significance at $p < 0.05$ based on the effective number of degrees of freedom (N^{eff}), following Xue et al.[10].

forcing. Li et al.[20] and Huyan et al.[19] have also suggested that the relationships between the EASM and ENSO, and between the EASM and Indian Ocean SST anomalies, have strengthened over the past decades. Recent studies also suggest that this enhanced QB periodicity in ENSO is linked to tropical North Atlantic SST variability associated with the state of the Atlantic Multidecadal Oscillation[19,20,22–26,41]. Our analysis further reveals that, alongside K–R wave amplification, the phase speed of baroclinic Rossby waves increased by approximately 70% over the SCTR region from the Early to the Late period, favouring the seasonal phase locking of ocean wave–driven tropical Indian Ocean warming with the EASM. Although variations in the observational data assimilated in reanalyses can introduce spurious variability, the observed intensification in QB-scale processes in this study is unlikely to result from such effects. In summary, this study identifies QB–scale Indian Ocean wave dynamics as a key driver of YRD variability at interannual timescale, highlighting a substantial oceanic control on the EASM (Fig. 8). These findings also highlight the importance of accurately representing Indian Ocean wave processes in climate models to improve prediction of monsoon-related hydrological extremes under ongoing climate change. Although the present study did not explore the contribution of anthropogenic climate change to the observed dynamical changes in the tropical Indian Ocean between the Early and Late periods, its role is likely significant and requires more thorough investigation.

The specific cause of the observed acceleration of baroclinic Rossby waves in tropical Indian Ocean during the Late period remains unresolved in this study and is an open question. Although we highlight enhanced ENSO-driven QB-scale WSC forcing as a plausible driver, this relationship requires further investigation. Moreover, QB–scale atmospheric forcing is closely coupled with local convection and precipitation variability associated with the changes in wave cycle itself, making it inherently difficult to distinguish cause from effect. Therefore, targeted numerical modelling experiments are needed to disentangle these processes. We also observe an increase in the wavelength of baroclinic Rossby waves accompanied by an increase in their phase speed. However, free-wave theory alone cannot account for the overall acceleration of the K–R wave cycle. In linear theory, the phase speed of equatorial Kelvin waves is independent of wavelength and depends solely on the equivalent depth. Therefore, classical free-wave theory is insufficient to explain the observed acceleration of the K–R wave cycle in such fully coupled and externally forced system, where nonlinear processes may also play an important role. It is also

https://doi.org/10.1038/s41467-026-70940-z

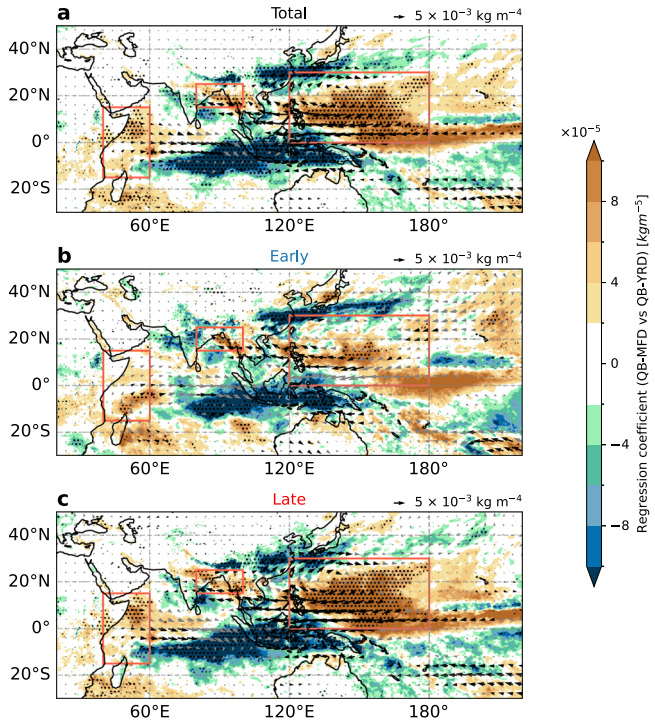

Fig. 6 | Column moisture flux divergence (MFD) and transport (MFT) associated with quasi-biennial timescale Yangtze River discharge (QB–YRD) derived from ERA5. QB–YRD regressed MFD (negative values indicate convergence leading to enhanced rainfall) (kg m^{-2} s^{-1}) and MFT (kg m^{-1} s^{-1}) during (**a**) total (1960–2024), **b** Early (1960–1991) and **c** Late (1992–2024) periods. Dotted regions and black arrows indicate statistical significance at $p < 0.05$ based on the effective number of degrees of freedom (N^{eff}), following Xue et al.[10]. The QB–YRD–regressed MFD and MFT identify the western Pacific subtropical high (WPSH), western tropical Indian Ocean (WTIO), and northern Bay of Bengal (nBOB) regions as the key moisture source areas. Their contributions are evident in both the Early and Late periods and become more pronounced during the Late period.

important to note that, due to the monthly temporal resolution of the ORAS5 and EN4 datasets, the present study could not resolve the detailed characteristics changes in equatorial Kelvin waves, although their amplification during the Late period is clearly evident.

Methods

Analysis of QB timescale

To analyse baroclinic Rossby wave dynamics, this study primarily followed the methodology of Menezes and Vianna[14]. Menezes and Vianna[14] utilised monthly sea level anomalies obtained from satellite observations to investigate baroclinic Rossby wave behaviour in the tropical Indian Ocean. We here used the SSH anomalies and the depth of the 20 °C isotherm (D20) from ORAS5 reanalysis. Since ORAS5 is a model-based product, we substantiated our analysis with D20 data from EN4, which is an observation-based product. While we primarily present SSH-based results in the main manuscript, both ORAS5 and EN4 datasets are in overall agreement regarding the key findings. SSH is emphasised here because it allows us to identify changes in Kelvin wave properties, which are not adequately captured through D20 variations alone. As suggested by Menezes and Vianna[14], QB (1.2–3 years or 14–36 months) variability predominantly reflects energetic first baroclinic-mode Rossby and Kelvin wave propagation across the tropical Indian Ocean basin. Therefore, this specific time band has been filtered using an FFT-based algorithm. To assess the significance of the QB frequency band in displaying baroclinic wave characteristics in the tropical Indian Ocean, Supplementary Fig. 1a, 1b, and 1c (upper panels) show the standard deviation of anomalies from ORAS5-SSH, ORAS5-D20, and EN4-D20, filtered into three distinct frequency bands: annual (10–14 months), QB (14–36 months), and ENSO-scale (36–96 months), after removal of the seasonal cycle. As evident from these figures, the standard deviation peaks in the QB band, indicating that baroclinic Rossby wave activity is most prominent at this timescale, consistent with Menezes and Vianna[14].

CEOF analysis and K–R wavecycle

To identify propagating wave characteristics during Early (1960–1991) and Late (1992–2024) period, we employed CEOF analysis on QB–timescale ORAS5–SSH, ORAS5–D20 and EN4–D20 following Menezes and Vianna[14]. CEOF analysis was conducted using the XEOFs package written in the Python programming language (https://xeofs.readthedocs.io/en/latest/). The phase speeds of CEOF1 are derived separately for the two periods (Fig. 2c, d). While the results indicate an overall increase in the dominant mode's phase speed during the Late period (Fig. 3a), the structural differences between the CEOF1 modes from the two periods suggest that further validation was needed. To further validate our findings, we performed a CEOF analysis over the entire study period (1960–2024), where the leading mode explained 47% of the total QB band variance. We then isolated time intervals where the CEOF1 amplitude exceeded the 25th percentile (denoting active wave propagation) and computed the phase speed in the SCTR for each of these eight active phases (Fig.3b and Supplementary Fig. 6). We selected this threshold to retain the full cycle of the K–R wave activity while excluding only the weakest period. Moreover, since CEOF1 explains a substantially larger proportion of variance than the second and third modes, this threshold ensures a robust representation of dominant wave dynamics (Supplementary Fig. 4).

The eight distinct phases of the K–R wave cycle are defined analogously to the eight phases of the Madden–Julian Oscillation (MJO) introduced by Wheeler and Hendon[42], based on the first two leading principal component planes. In the present study, using CEOF analysis, the two-dimensional phase space is constructed from the real and imaginary components of the CEOF1. Temporal variations in the real and imaginary components of the CEOF1 describe the propagation of the dominant traveling mode across the basin. The phase space is divided into eight 45° angular sectors, each representing one phase of the K–R wave cycle. To construct composites of QB-SSH anomalies for these eight phases, we consider months for which the amplitude of CEOF1 $\left(\sqrt{\mathrm{CEOF1}_{\mathrm{real}}^2 + \mathrm{CEOF1}_{\mathrm{imag}}^2}\right)$ exceeds the 25th percentile. This threshold is chosen to retain the complete K–R wave cycle while excluding only the weakest periods of activity.

Mixed layer heat budget

$$\frac{\partial T_a}{\partial t} = \underbrace{\frac{q_0 - q_{-h}}{\rho c_p h}}_{\text{Surface heat flux}} - \underbrace{v_a \cdot \nabla T_a}_{\text{Horizontal advection}} - \underbrace{\frac{1}{h}\nabla \cdot \int_{-h}^{0} \hat{v}\,\hat{T}\,dz}_{\text{Horizontal eddy heat transport}} - \underbrace{\frac{T_a - T_{-h}}{h}\left(\frac{\partial h}{\partial t} + v_{-h} \cdot \nabla h + w_{-h}\right)}_{\text{Entrainment}} - \underbrace{\frac{1}{h} K_v \frac{\partial T}{\partial z}\Big|_{z=-h}}_{\text{Vertical diffusion}} \quad (1)$$

The heat budget analysis conducted in this study followed the approach of Moisan and Niiler[43], using monthly data from ORAS5 reanalysis. To distinguish between surface and subsurface influences on mixed layer temperature, we categorised the budget terms into three components: **surface processes**, comprising net surface heat flux, horizontal advection and horizontal eddy heat transport within the mixed layer; **unresolved subsurface processes**, inferred as the residual between total temperature tendency and surface processes; **vertical processes**, including vertical entrainment and turbulent

https://doi.org/10.1038/s41467-026-70940-z

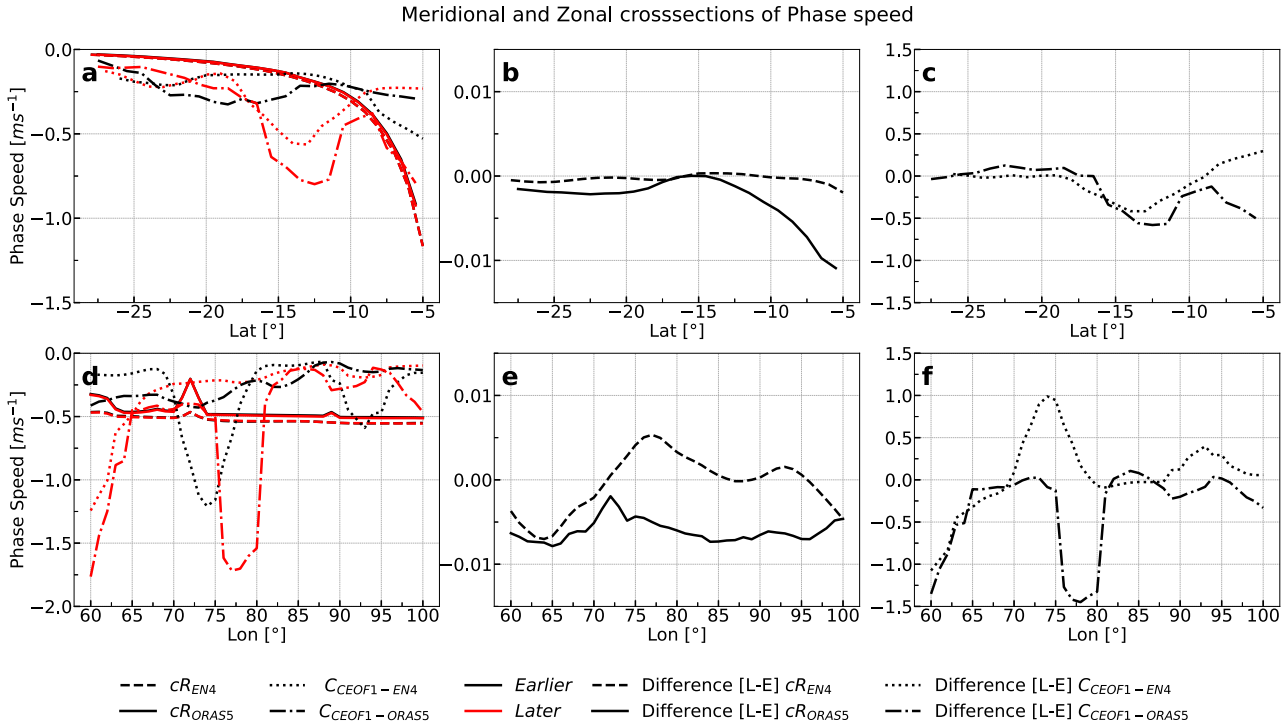

Fig. 7 | Changes in the first baroclinic-mode free Rossby wave phase speeds due to stratification changes and its comparison with leading complex EOF (CEOF1) mode phase speeds derived from ORAS5–SSH and EN4–D20. First baroclinic-mode free Rossby wave phase speeds [m s^{-1}] were computed using the WKBJ approximation (cR_{EN4} and cR_{ORAS5}) and compared between the Early (1960–1991) and Late (1992–2024) periods, along with CEOF1 phase speeds ($C_{CEOF1-EN4}$ and $C_{CEOF1-ORAS5}$). (**a, d**) Mean zonally averaged (60°E–100°E) and meridionally averaged (12°S–5°S) profiles of first baroclinic-mode free Rossby wave (cR) and CEOF1 phase speeds [m s^{-1}]. (**b**, **e**) Meridional and zonal sections showing differences in first baroclinic-mode free Rossby wave phase speed due to changes in squared buoyancy frequency (N^2 [s^{-2}]), (**c**, **f**) Meridional and zonal sections showing differences in westward phase speed [m s^{-1}] of the CEOF1 mode computed from ORAS5–SSH and EN4–D20, respectively.

diffusion. The mixed layer depth used in this study was derived from ORAS5 reanalysis, based on a density difference criterion of 0.03 kg m^{-3}. Vertical velocity at the mixed layer base has been parameterized using the rate of change of D20. The penetrative shortwave radiation in the mixed layer was parameterized using a two-exponential attenuation formulation[44]: $q_{-h} = q_{sw}\left[R\,e^{-z/k_1} + (1-R)\,e^{-z/k_2}\right]$, where q_{sw} is the surface shortwave radiation, z is depth, $R = 0.62$ is the fractional contribution of the fast-decaying component, $k_1 = 0.60m$ is the shallow attenuation scale, and $k_2 = 20m$ is the deep attenuation scale. Vertical turbulent mixing in the base of the mixed layer was calculated using a constant vertical diffusivity of $K_v = 10^{-5}\mathrm{m}^2\mathrm{s}^{-1}$. Three components of the vertical entrainment terms i.e., ENT1, ENT2, and ENT3 represent entrainment associated with the local mixed-layer tendency, horizontal mixed-layer advection, and vertical heat advection, respectively. Anomalous ENT1 term was further decomposed using $ENT1' = \frac{\partial h}{\partial t}GTD' + \frac{\partial h'}{\partial t}\overline{GTD} + \frac{\partial h'}{\partial t}GTD'$ where $GTD = \frac{T_a - T_{-h}}{h}$ represents the vertical temperature gradient across the mixed layer.

Estimation of first baroclinic-mode free Rossby wave phase speed

The vertical modes were calculated using the Dynmodes package (available at https://www.eoas.ubc.ca/~sallen/AIMS-workshop/modules/dynmodes.html) from stratification profiles, represented by the squared buoyancy frequency N^2 (z) (s^{-2}). The modes were computed independently at each longitude and latitude using mean-state stratification for the Early (1960–1991) and Late (1992–2024) periods. Using the WKBJ approximation, we estimated the first baroclinic-mode gravity wave speed from the mean buoyancy frequency (N^2) profile down to a 3,500-m depth at each grid point. Based on this gravity wave speed, we then computed the first baroclinic-mode free Rossby wave phase speed using the standard dispersion relation under the assumption of zero background zonal current. Notably, the changes in stratification and corresponding changes in the theoretical free baroclinic Rossby wave speed, differed substantially between the model-based ORAS5 SSH and the observation-based EN4 D20 datasets. Although, the observed CEOF1 phase speed changes were consistent across both datasets in the western SCTR.

Phase coherence estimation

To quantify the phase relationship between QB–scale wind stress curl and QB–scale SSH and D20 during the Early and Late periods, we computed the phase coherence using the Hilbert transform-based analytic signal approach. If $x(t)$ and $y(t)$ are two zero-mean filtered time series. The analytic signal of each filtered time series was constructed using the Hilbert transform:

$$z(t) = x(t) + i\mathcal{H}[x(t)] = A_x(t)e^{i\phi_x(t)} \tag{2}$$

$$w(t) = y(t) + i\mathcal{H}[y(t)] = A_y(t)e^{i\phi_y(t)} \tag{3}$$

where $\mathcal{H}[\cdot]$ denotes the Hilbert transform, $A(t)$ is the instantaneous amplitude, and $\phi(t)$ is the instantaneous phase. The phase difference $\Delta\phi(t) = \phi_x(t) - \phi_y(t)$ was then computed, and the phase coherence γ was estimated as:

$$\gamma = \left| \frac{1}{N} \sum_{t=1}^{N} e^{i\Delta\phi(t)} \right| \tag{4}$$

where N is the total number of time steps. The phase coherence $\gamma \in [0, 1]$, with $\gamma = 1$ indicating perfect phase locking and $\gamma = 0$ implying no phase relationship.

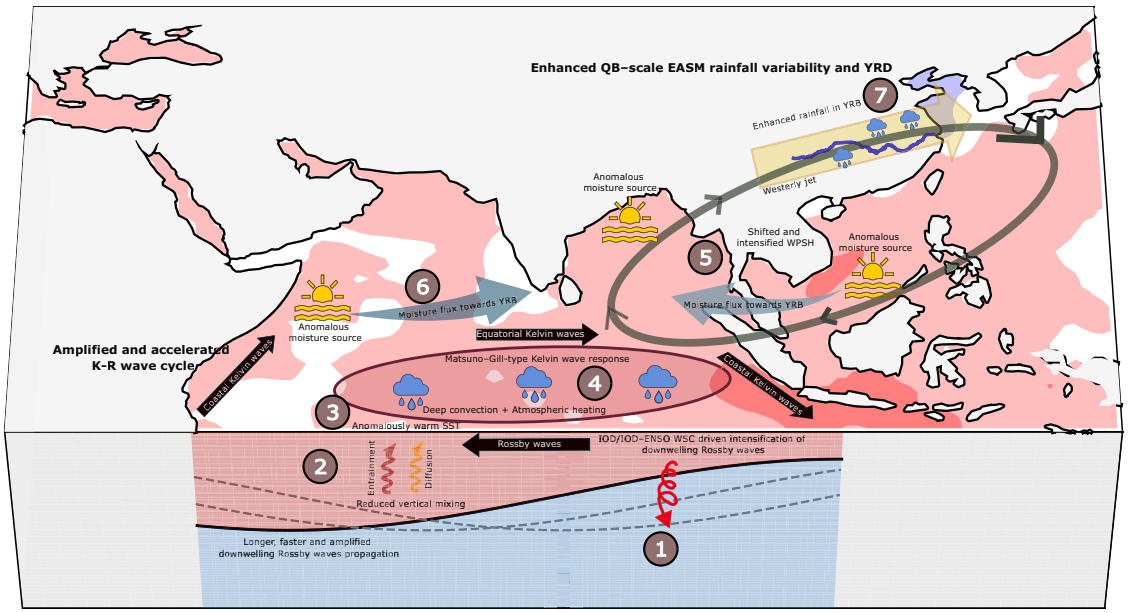

Fig. 8 | Schematic diagram explaining the mechanism for the enhancement of quasi-biennial timescale Yangtze River discharge (QB–YRD) variability during the Late period (1992–2024) compared to the Early period (1960–1991). The numbers denote the sequence of processes responsible for this enhancement. (1) Post–positive Indian Ocean Dipole or combined El Niño–Southern Oscillation and Indian Ocean Dipole (IOD/ENSO–IOD) related windstress curl forcing intensifies the downwelling Rossby wave component of the Kelvin–Rossby (K–R) wave cycle. (2) The forced downwelling Rossby waves propagate westward faster and reflect as an equatorial Kelvin wave, and this acceleration of the K–R waves favors seasonal phase locking with the East Asian summer monsoon (EASM) during the Late period. (3) The longer, amplified, and faster downwelling Rossby waves at CEOF1 phase 6 significantly reduce vertical entrainment and diffusion-driven mixing in the western–central Indian Ocean. (4) The reduced vertical mixing induces anomalously warm SST and associated atmospheric deep convective activity over the region. (5) The deep convective clouds and associated condensation heating induce a Matsuno–Gill-type atmospheric Kelvin wave response, (6) which further intensifies and shifts the western Pacific subtropical high (WPSH) anticyclone. (7) The western flank of this intensified anomalous anticyclone transports more moisture toward the Yangtze River basin (YRB), causing heavy precipitation over the region during the EASM. Following negative IOD/ENSO–IOD events, a similar sequence of processes associated with upwelling K–R waves leads to drought conditions in the basin. Overall, intensified and faster K–R waves at QB timescales enhance QB-scale EASM rainfall variability and the associated river discharge in the YRB.

Statistical significance testing

The effective sample size (N^{eff}) for QB–scale correlation is derived based on following equation[24],

$$\frac{1}{N^{\text{eff}}} \approx \frac{1}{N} + \frac{2}{N}\sum_{j=1}^{N}\frac{N-j}{N}\rho_{XX}(j)\rho_{YY}(j) \quad (5)$$

Where N, $\rho_{XX}(j)$ *and* $\rho_{YY}(j)$ denote the effective sample size and auto correlations of timeseries X and Y at time lag j respectively. A Student's t-test was applied to assess the statistical significance of the difference in means between the two samples.

Data availability

The ORAS5 ocean reanalysis data used in this study were obtained from the European Centre for Medium-Range Weather Forecasts (ECMWF)[45]. The specific ORAS5 variables analysed included SSH, SST, ocean currents, heat flux components, and wind stress terms. These datasets are publicly available from the Copernicus Climate Data Store at https://cds.climate.copernicus.eu/. Monthly ocean temperature and salinity profiles were obtained from the EN4 dataset (version 4.2.2), provided by the UK Met Office[46]. Wind stress curl was calculated using the ERA5 monthly reanalysis dataset from the European Centre for Medium-Range Weather Forecasts[47]. YRD data recorded at the Datong station were obtained from the Ministry of Water Resources of the People's Republic of China. Niño 3.4 (area–averaged SST anomaly over 5°S–5°N, 170°–120°W) and DMI (area–averaged SST anomaly difference between the western equatorial Indian Ocean: 50°–70°E, 10°S–10°N and the south-eastern equatorial Indian Ocean: 90°–110°E, 10°S–0°) were obtained from the NOAA Physical Sciences Laboratory (https://psl.noaa.gov/data/timeseries/month/), derived using the HadISST dataset[48]. The IOB index was computed using monthly ERSSTv5 data[49] by differencing the average SSTs over the region 40°E–100°E and 20°S–20°N. The north tropical Atlantic (NTA) (area–averaged SST anomalies over 0°–15°N, 90°W–20°E) index was calculated using ERSSTv5 data. The WPSH index in this study was calculated from ERA5 500-hPa geopotential height anomalies over the subtropical western North Pacific region (e.g., 10°–40°N, 110°E–180°E). Gridded precipitation data for the Chinese mainland based on gauge observations (CHM rainfall) were obtained from Han et al[50]. The Global Precipitation Climatology Centre (GPCC) precipitation data used in this study were provided by the Deutscher Wetterdienst (DWD). The GPCC Full Data Monthly Product Version 2020, based on rain gauge observations, is publicly available and can be accessed at https://www.dwd.de/EN/ourservices/gpcc/gpcc.html.

Code availability

Code used in this study is publicly available via Zenodo at URL https://doi.org/10.5281/zenodo.18786090.

References

1. Wang, Y., Wu, B. & Zhou, T. Maintenance of Western North Pacific anomalous anticyclone in boreal summer by wind-induced moist enthalpy advection mechanism. *J. Clim.* **35**, 4499–4511 (2022).
2. Zhou, Z. Q., Xie, S. P. & Zhang, R. Historic Yangtze flooding of 2020 tied to extreme Indian Ocean conditions. *Proc. Natl. Acad. Sci. Usa.* **118**, e2022255118 (2021).
3. Zhu, Z., Feng, Y., Jiang, W., Lu, R. & Yang, Y. The compound impacts of sea surface temperature modes in the Indian and North Atlantic oceans on the extreme precipitation days in the Yangtze River Basin. *Clim. Dyn.* **61**, 3327–3341 (2023).

4. Gong, Y. et al. Synchronous characteristics of precipitation extremes in the Yangtze and Murray-Darling river basins and the role of ENSO. *J. Meteorological Res.* **35**, 282–294 (2021).
5. Zhang, W. et al. Unraveling El Niño's impact on the East Asian Monsoon and Yangtze River summer flooding. *Geophys. Res. Lett.* **43**, 11,375–11,382 (2016).
6. Wu, X., Wang, L., Niu, Z., Jiang, W. & Cao, Q. More extreme precipitation over the Yangtze River Basin, China: Insights from historical and projected perspectives. *Atmos. Res.* **292**, 106883 (2023).
7. Liu, S. et al. Are only floods with large discharges threatening? Flood characteristics evolution in the Yangtze River Basin. *Geosci. Lett.* **8**, 1–3 (2021).
8. Pan, C. et al. The characteristics of the Yangtze Flooding During 1998 and 2020 based on atmospheric water tracing. *Geophys. Res. Lett.* **50**, e2023GL104195 (2023).
9. Wu, J. et al. Boosting effect of strong western pole of the Indian Ocean Dipole on the decay of El Niño events. *NPJ Clim. Atmos. Sci.* **7**, 1–11 (2024).
10. Sun, S., Fang, Y., Zu, Y., Liu, L. & Li, K. Increased occurrences of early Indian Ocean Dipole under global warming. *Sci. Adv.* **8**, (2022).
11. Wang, J., Zhang, S., Jiang, H. & Yuan, D. Indian Ocean Basin Warming in 2020 Forced by Thermocline Anomalies of the 2019 Indian Ocean Dipole. *J. Clim.* **37**, 145–163 (2023).
12. McPhaden, M. J. & Nagura, M. Indian Ocean dipole interpreted in terms of recharge oscillator theory. *Clim. Dyn.* **42**, 1569–1586 (2014).
13. Zhang, Y. & Du, Y. Oceanic Rossby waves induced two types of ocean–atmosphere response and opposite indian ocean dipole phases. *J. Clim.* **35**, 3927–3945 (2022).
14. Menezes, V. V. & Vianna, M. L. Quasi-biennial Rossby and Kelvin waves in the South Indian Ocean: Tropical and subtropical modes and the Indian Ocean Dipole. *Deep Sea Res. Part II: Topical Stud. Oceanogr.* **166**, 43–63 (2019).
15. Qiu, B., Miao, W. & Müller, P. Propagation and Decay of Forced and Free Baroclinic Rossby Waves in Off-Equatorial Oceans. *J. Phys. Oceanogr.* **27**, 2405–2417 (1997).
16. Jury, M. R. & Huang, B. The Rossby wave as a key mechanism of Indian Ocean climate variability. *Deep Sea Res. Part I: Oceanographic Res. Pap.* **51**, 2123–2136 (2004).
17. Meehl, G. A. The annual cycle and interannual variability in the tropical pacific and indian ocean regions. *Mon. Weather Rev.* **115**, 27–50 (1987).
18. Meehl, G. A. The South Asian monsoon and the tropospheric biennial oscillation. *J. Clim.* **10**, 1921–1943 (1997).
19. Huyan, L. et al. The impact of layer perturbation potential energy on the east asian summer monsoon. *J. Clim.* **30**, 7087–7103 (2017).
20. Li, J., Wu, Z., Jiang, Z. & He, J. Can Global Warming Strengthen the East Asian Summer Monsoon? *J. Clim.* **23**, 6696–6705 (2010).
21. Zhang, Y. et al. Characteristics of boreal summer compound hot-drought events in the Yangtze River Valley and relationships with Indian Ocean Sea surface temperature. *Clim. Dyn.* **63**, 1–17 (2025).
22. Wang, L., Yu, J. Y. & Paek, H. Enhanced biennial variability in the Pacific due to Atlantic capacitor effect. *Nat. Commun.* **8**, 14887 (2017). *2017 8:1*.
23. Wu, M. et al. Recent enhancement in co-variability of the western north pacific summer monsoon and the equatorial zonal wind. *Adv. Atmos. Sci.* **40**, 1597–1616 (2023). *2023 40:9*.
24. Xue, J., Luo, J. J., Zhang, W. & Yamagata, T. ENSO–IOD inter-basin connection is controlled by the atlantic multidecadal oscillation. *Geophys. Res. Lett.* **49**, e2022GL101571 (2022).
25. Wu, M. & Wang, L. Enhanced correlation between ENSO and western North Pacific monsoon during boreal summer around the 1990s. *Atmos. Ocean. Sci. Lett.* **12**, 376–384 (2019).
26. Chen, B., Wang, L. & Wu, M. Contrasting the Indian and western North Pacific summer monsoons in terms of their intensity of interannual variability and biennial relationship with ENSO. *Atmos. Ocean. Sci. Lett.* **13**, 462–469 (2020).
27. Ge, H., Zhu, L. & Mao, B. Hydrological drought in the lower reaches of the Yangtze River (China): a 70-year data analysis. *Front. Mar. Sci.* **12**, 1534674 (2025).
28. Jarugula, S. & McPhaden, M. J. Indian ocean dipole affects eastern tropical atlantic salinity through congo river basin hydrology. *Commun. Earth Environ.* **4**, 1–9 (2023).
29. Chelton, D. B. & Schlax, M. G. Global observations of oceanic Rossby waves. *Science (1979)* **272**, 234–238 (1996).
30. Masumoto, Y. & Meyers, G. Forced Rossby waves in the southern tropical Indian Ocean. *J. Geophys. Res. Oceans* **103**, 27589–27602 (1998).
31. Chelton, D. B., Deszoeke, R. A., Schlax, M. G., El Naggar, K. & Siwertz, N. Geographical variability of the first baroclinic rossby radius of deformation. *J. Phys. Oceanogr.* **28**, 433–460 (1998).
32. Foltz, G. R., Vialard, J., Kumar, B. P. & Mcphaden, M. J. Seasonal Mixed Layer Heat Balance of the Southwestern Tropical Indian Ocean. *J. Clim.* **23**, 947–965 (2010).
33. Halkides, D. & Lee, T. Mechanisms controlling seasonal mixed layer temperature and salinity in the Southwestern Tropical Indian Ocean. *Dyn. Atmospheres Oceans* **51**, 77–93 (2011).
34. Yokoi, T., Tozuka, T. & Yamagata, T. Seasonal and Interannual Variations of the SST above the Seychelles Dome. *J. Clim.* **25**, 800–814 (2012).
35. Kumar, P. et al. Processes of interannual mixed layer temperature variability in the thermocline ridge of the Indian Ocean. *Clim. Dyn.* **43**, 2377–2397 (2014).
36. Soares, S. M., Richards, K. J., Bryan, F. O. & Yoneyama, K. On the seasonal cycle of the tropical south indian ocean. part I: Mixed layer heat and salt budgets. *J. Clim.* **32**, 1951–1972 (2019).
37. Xie, S. P. et al. Indian Ocean Capacitor Effect on Indo–Western Pacific Climate during the Summer following El Niño. *J. Clim.* **22**, 730–747 (2009).
38. Matsuno, T. Quasi-geostrophic motions in the equatorial area. *J. Meteorological Soc. Jpn. Ser. II* **44**, 25–43 (1966).
39. Ferster, B. S., Fedorov, A. V., Guilyardi, E. & Mignot, J. The Effect of Indian Ocean temperature on the pacific trade winds and ENSO. *Geophys. Res. Lett.* **50**, e2023GL103230 (2023).
40. Hu, K., Huang, G., Qu, X. & Huang, R. The impact of Indian Ocean variability on high temperature extremes across the southern Yangtze River valley in late summer. *Adv. Atmos. Sci.* **29**, 91–100 (2011).
41. Gan, Q., Wang, L., Leung, J. C. H., Weng, J. & Zhang, B. Recent weakening relationship between the springtime Indo-Pacific warm pool SST zonal gradient and the subsequent summertime western Pacific subtropical high. *Int. J. Climatol.* **42**, 10173–10194 (2022).
42. Wheeler, M. C. & Hendon, H. H. An all-season real-time multivariate MJO index: Development of an index for monitoring and prediction. *Mon. Weather Rev.* **132**, 1917–1932 (2004).
43. Moisan, J. R. & Niiler, P. P. The Seasonal Heat Budget of the North Pacific: Net Heat Flux and Heat Storage Rates (1950–1990). *J. Phys. Oceanogr.* **28**, 401–421 (1998).
44. Paulson, C. A. & Simpson, J. J. Irradiance measurements in the upper ocean. *JPO* **7**, 952–956 (1977).
45. Zuo, H., Balmaseda, M. A., Tietsche, S., Mogensen, K. & Mayer, M. The ECMWF operational ensemble reanalysis-analysis system for ocean and sea ice: A description of the system and assessment. *Ocean Sci.* **15**, 779–808 (2019).
46. Good, S. A., Martin, M. J. & Rayner, N. A. EN4: Quality controlled ocean temperature and salinity profiles and monthly objective analyses with uncertainty estimates. *J. Geophys. Res. Oceans* **118**, 6704–6716 (2013).
47. Hersbach, H. et al. The ERA5 global reanalysis. *Q. J. R. Meteorolog. Soc.* **146**, 1999–2049 (2020).

48. Rayner, N. A. et al. Global analyses of sea surface temperature, sea ice, and night marine air temperature since the late nineteenth century. *J. Geophys. Res.: Atmospheres* **108**, 4407 (2003).
49. Huang, B. et al. Extended reconstructed sea surface temperature, version 5 (ERSSTv5): upgrades, validations, and intercomparisons. *J. Clim.* **30**, 8179–8205 (2017).
50. Han, J. et al. A new daily gridded precipitation dataset for the Chinese mainland based on gauge observations. *Earth Syst. Sci. Data* **15**, 3147–3161 (2023).

Acknowledgements

This research was supported from program/project titled "KUDOS (Korea-US Indian Ocean Science program)" and "KIOS (Korea Indian Ocean Study)" by Korea Institute of Marine Science and Technology Promotion (KIMST) funded by the Ministry of Oceans and Fisheries, Korea (RS-2022-KS221662; PM65240). This research was conducted as part of the 'UN Decade Implementation Research Group project (RS-2023-00256732)', funded by the Ministry of Oceans and Fisheries, Korea. This research was also supported by the National Research Foundation of Korea (NRF) grant funded by the Korea government (MSIT) (No. RS-2024-00405801 and NRF-2022R1A2C1003128). PMEL contribution number 5850. We sincerely thank the three anonymous reviewers for their insightful comments and constructive suggestions, which substantially improved the scientific quality and clarity of this manuscript.

Author contributions

M.J.M., S.N., and D.K. conceived the study. P.D. and J.S.S. carried out the analyses and prepared the initial draft of the manuscript. R.M.K. provided valuable guidance on the analysis and presentation. All authors contributed to the interpretation of the results and to revising the manuscript for publication.

Competing interests

The authors declare no competing interests.

Additional information

Supplementary information The online version contains supplementary material available at https://doi.org/10.1038/s41467-026-70940-z.

Correspondence and requests for materials should be addressed to SungHyun Nam or Michael J. McPhaden.

Peer review information *Nature Communications* thanks Nathaniel Bindoff, Boualem Khouider, and Jianping Li for their contribution to the peer review of this work. A peer review file is available.